Hybrid Perovskites

Control of Perovskite Crystal Growth by Methylammonium Lead Chloride Templating

Andreas Binek[+], Irene Grill[+], Niklas Huber[+], Kristina Peters, Alexander G. Hufnagel, Matthias Handloser, Pablo Docampo, Achim Hartschuh, and Thomas Bein*[a]

Abstract: State-of-the-art solar cells based on methylammonium lead iodide (MAPbI$_3$) now reach efficiencies over 20%. This fast improvement was possible with intensive research in perovskite processing. In particular, chloride-based precursors are known to have a positive influence on the crystallization of the perovskite. Here, we used a combination of in-situ X-ray diffraction and charge-transport measurements to understand the influence of chloride during perovskite crystallization in planar heterojunction solar cells. We show that MAPbCl$_3$ crystallizes directly after the deposition of the starting solution and acts as a template for the formation of MAPbI$_3$. Additionally, we show that the charge-carrier mobility doubles by extending the time for the template formation. Our results give a deeper understanding of the influence of chloride in the synthesis of MAPbI$_3$ and illustrate the importance of carefully controlling crystallization for reproducible, high-efficiency solar cells.

With rising global energy demands and the decline of fossil fuels reserves, there is a great need to develop renewable energy resources. Lately, solar cells based on organic-inorganic trihalide perovskites, for example, (CH$_3$NH$_3$)PbI$_3$, have emerged as a highly efficient and inexpensive photovoltaic technology.[1–4] Through optimization of the fabrication processes,[5–7] the annealing process,[8–9] and the interfaces,[10] perovskite solar cells have already exceeded 20% power conversion efficiency (PCE).[11] Recently, several novel crystallization methods have been exploited to fabricate perovskite photovoltaic devices with high and reproducible performance.[12–13] In particular, previous studies show that control of the macroscopic morphology and the crystalline domain size has a strong influence on

the resulting device performance.[14–16] Hence, understanding the crystallization mechanism of the active layer is a crucial factor. In grain boundaries and defects, traps for the photoexcited species are located and recombination can occur.[17] Thus, a good strategy to maximize device efficiency is the reduction of the number of grain boundaries in the perovskite layer by tuning the deposition technique.[18] A common approach to improve the performance of perovskite solar cells is the use of a chloride-based precursor in the casting solution. In particular, lead chloride (PbCl$_2$) and methylammonium iodide (MAI) mixtures lead to highly efficient devices when employed in planar heterojunction solar cells.[19] This enhancement is generally attributed to the formation of bigger crystal domains of the perovskite compared to other precursors and the related reduction of grain boundaries and defects in the bulk material.[16] However, the role of chloride during the crystallization process is still unclear, with many groups reporting no or only small amounts of chloride in the final structure.[20–23] Thus, understanding the crystallization mechanism and, therefore, gaining additional handles to tune the crystal morphology of these systems can open up new strategies to maximize the device performance. Here, we investigate the crystallization of the perovskite immediately after deposition in order to understand and control the crystallization kinetics of the system. Our in-situ X-ray diffraction measurements show that initially MAPbCl$_3$ crystallizes on the substrates to be fully converted into MAPbI$_3$ after a certain time under heating. Furthermore, we show the positive influence of the slow evaporation of the solvent on the crystal size, morphology, and also on the charge-carrier mobility in the perovskite layer. Our results help to understand the influence of chloride during the crystallization process of the perovskite and the origin of the improved performance of the system.

The MAPbI$_3$ samples were prepared according to the synthesis route of Eperon et al.[8] In short, a mixture of lead chloride (PbCl$_2$) and methylammonium iodide (MAI) was dissolved at a ratio of 1:3, and was then spin-coated on a TiO$_2$-covered fluorine-doped tin oxide (FTO) substrate. Afterwards, the sample was kept at room temperature (RT) for different times to allow for the slow evaporation of the residual solvent, and then heated to different temperatures to complete the conversion to the MAPbI$_3$ crystal phase. With this procedure we enabled slow formation of the perovskite, leading to uniform crystallites. In order to examine the influence of different evaporation times of the solvent at RT on the perovskite morphology,

[a] A. Binek,[+] I. Grill,[+] N. Huber,[+] K. Peters, A. G. Hufnagel, Dr. M. Handloser, Dr. P. Docampo, Prof. A. Hartschuh, Prof. T. Bein
Department of Chemistry and Center for NanoScience (CeNS)
University of Munich (LMU)
Butenandtstr. 5–13 (Haus E), 81377 Munich (Germany)
E-mail: bein@lmu.de

[+] These authors contributed equally to this work.

Supporting information for this article can be found under http://dx.doi.org/10.1002/asia.201501379.

This manuscript is part of a special issue on energy conversion and storage. Click here to see the Table of Contents of the special issue.

cross-sections were prepared (Figure 1). Short exposure times between 1 min and 20 min resulted in crystallites that are not uniform in size and shape, and a large number of grain boundaries are visible. In contrast, the SEM images of samples with a longer crystallization time show larger and more uniform crystallites, and consequently a reduction of grain boundary density.

To substantiate the uniformity of the MAPbI$_3$ crystals, smooth cross sections showing high contrast were also prepared with a focused ion beam (FIB). In the FIB cross-sections (Figure 1 b) the noticeable difference between fast and slow evaporation of the solvent is even more visible. The 5 min sample exhibits a rough surface due to non-uniform crystal formation. In comparison, the 40 min sample shows a regular brick-like morphology of the perovskite on the substrate. In order to further understand the crystallization and the influence of the different temperature treatments during the synthesis, in-situ X-Ray diffraction measurements (XRD) were performed under a nitrogen atmosphere with freshly spin-coated samples. Additionally, we investigated the effect of heating steps on the perovskite crystal structure; such steps are often used to achieve highly efficient devices for a range of exposure times (Figure 2). In the first XRD pattern, after 5 min at RT, an intense reflection at around 16° 2θ is observed. Over time, an additional reflection at 14° 2θ appears and slowly increases at RT. The first reflection at higher angles (16° 2θ) is attributed to the (200) plane of the MAPbCl$_3$ perovskite structure, while the second reflection (14° 2θ) is attributed to the (002) plane of MAPbI$_3$ (Figure 2 d); no shift is present in either reflection,

therefore ruling out MAPbI$_{3-x}$Cl$_x$ mixed phases. The broad reflection between 11.2 and 12.6° 2θ is likely the result of the formation of PbI$_n^{(2-n)}$ complexes, which arise as a result of employing non-stoichiometric perovskite mixtures with an excess of the organic cation.[24] The difference between both structures is not only the halide but also the arrangement of the PbX$_6$ octahedra. Heating to 90 °C leads to a reversal of reflection intensity of both perovskite structures, and thus conversion from one structure to the other. Thereby, the intensity of MAPbCl$_3$ is quickly decreased while the reflection of MAPbI$_3$ gains in intensity. Furthermore, the second reflection of the iodide perovskite at around 28° 2θ also increases during the heat treatment. In the following two temperature steps (Figure 2 c), the intensity of MAPbCl$_3$ reflections is further decreased and the orientation of the MAPbI$_3$ crystals is enhanced as the number of reflections is reduced, and only reflections arising from c-axis orientation remain. After cooling down to RT, only two reflections are observed, indexed as (001) and (002) from MAPbI$_3$, indicating that the crystals exhibit a preferred orientation along the c-axis and therefore parallel to the substrate. The same orientation is also observed in samples having been exposed to different evaporation times at RT, as shown in Figure S1 in the Supporting Information. From a crystallographic point of view the samples are very similar, however, the cross-sections show different morphologies.

Crystallization of a material from a solution can occur by cooling down the solution or through evaporation of the solvent.[25] In the case of the one-step synthesis route for MAPbI$_3$, supersaturation is induced by evaporating the solvent. This is
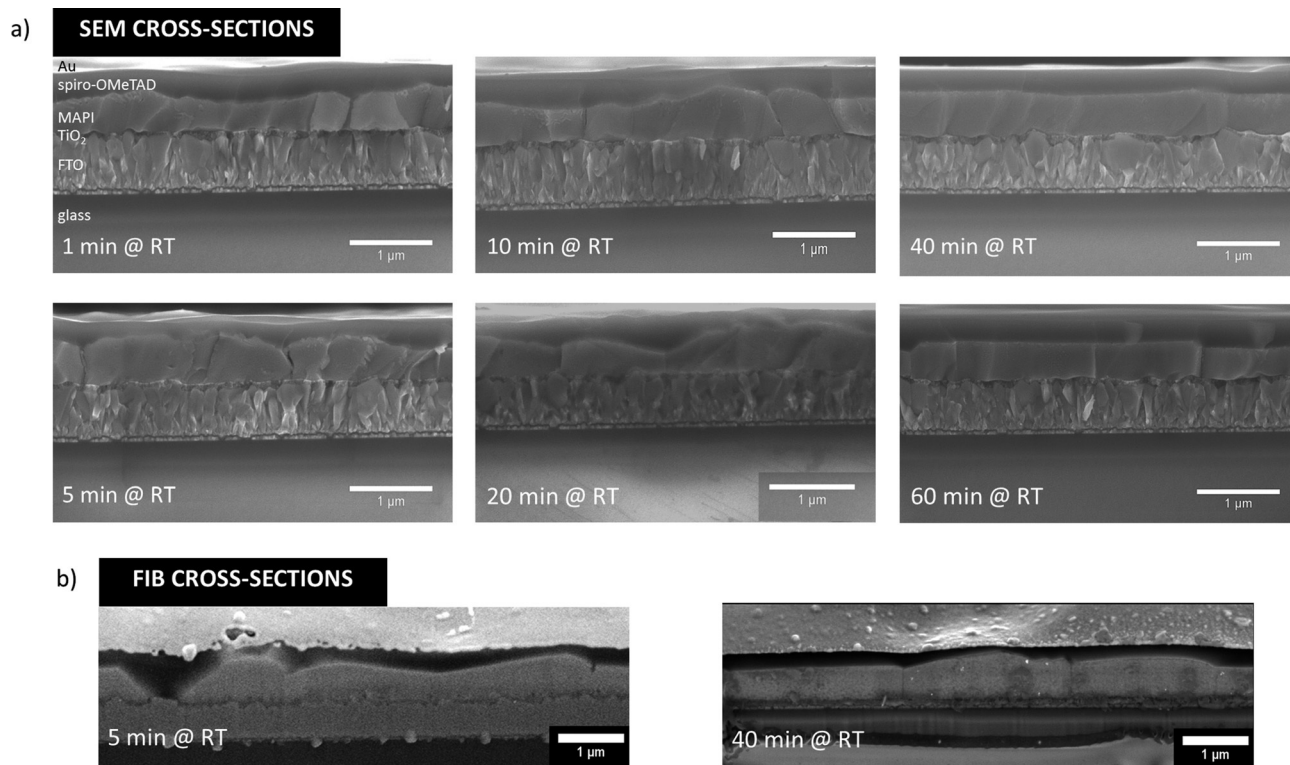
Figure 1. SEM images of cross-sections of samples with different evaporation times at RT (a) and SEM images of FIB cross-sections of a 5 min and a 40 min sample, respectively (b).
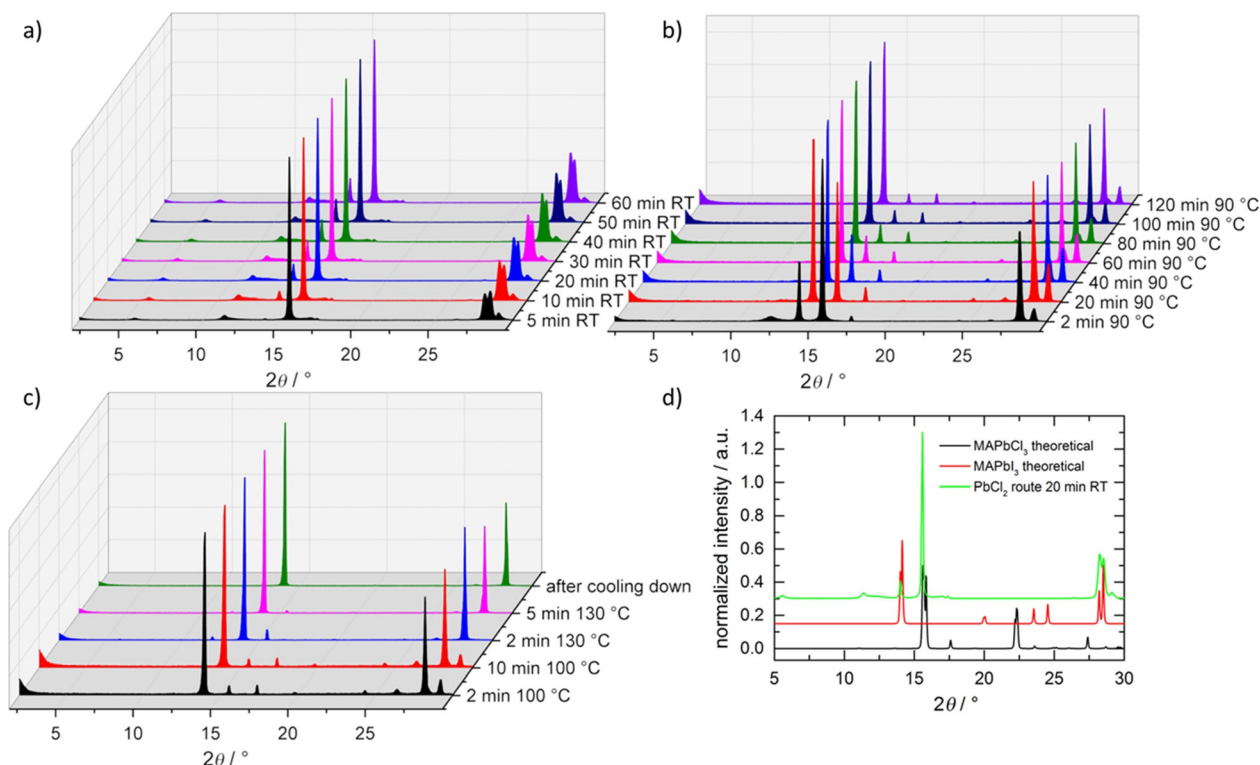
Figure 2. In-situ X-ray diffraction measurements with samples prepared according to the PbCl$_2$ route. XRD patterns for the RT step from 5 min to 60 min (a), 90 °C step from 2 min to 120 min (b), 100 °C/130 °C at different times and after cooling down (c). Theoretical patterns of MAPbI$_3$ and MAPbCl$_3$ compared with XRD pattern of the sample after 20 min at RT (d).

achieved through spinning of the substrate, which then leads to the formation of the nuclei. Afterwards, the crystallites grow due to the heating of the substrate. The fact that chloride, which improves the crystal quality of the perovskite,[26] is not incorporated into the structure of MAPbI$_3$, indicates that its effect must take place during the crystallization process.

The crystallization order of the two perovskite structures can be explained with the Ostwald–Volmer rule, which states that the system with the lower density crystallizes first.[27] Here, the density of MAPbCl$_3$[28] was estimated as 1.576 g cm^{-3}, while a value of 4.119 g cm^{-3} was obtained for the MAPbI$_3$[29] compound, and therefore the chloride-containing material is expected to crystallize first, as observed experimentally. We show a schematic of the proposed mechanism in Figure 3. Here, the sample is left at RT for the slow evaporation of the solvent, where MAPbCl$_3$ forms on the surface and acts as a template

for MAPbI$_3$. Additionally, some crystallites of MAPbI$_3$ emerge during the RT treatment as observed in the in-situ XRD. These can then act as seeds for the formation of the MAPbI$_3$ layer while heating up the system. Over time, the solvent as well as the excess of MA and chloride are evaporated, and highly oriented MAPbI$_3$ crystals are formed on the surface of the substrate with the orientation induced by the MAPbCl$_3$ template. With this crystallization mechanism, the morphological differences in the SEM cross-sections can be explained with the time required by the MAPbCl$_3$ template to form on the surface. A short time of 5 min at RT appears to be insufficient to create an oriented and fully formed MAPbCl$_3$ template. Therefore, in this case, the deposition of MAPbI$_3$ during the heat treatment leads to less uniform and smaller crystals. The difference between samples treated for 5 min and 40 min at room temperature was further investigated by incorporating the resulting
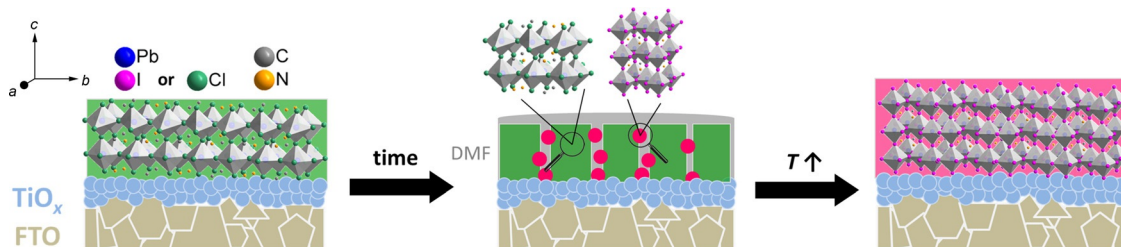
Figure 3. Schematic mechanism of the crystallization of the MAPbI$_3$ perovskite based on the PbCl$_2$ synthesis route in accordance with the Ostwald–Volmer rule.

perovskite layers in a planar heterojunction photovoltaic device architecture with TiO_2 and spiro-OMeTAD serving as the charge extraction contacts.[30] The current/voltage curves and the efficiency distributions of the devices are displayed in Figure 4a and 4b, respectively. We show that the film treated for 40 min at RT exhibits enhanced PCE values in comparison to the film treated for 5 min at RT. We attribute this difference to the higher crystallinity and more uniform size distribution of crystals within the film during the $MAPbCl_3$ template-assisted growth process, as illustrated by our in-situ XRD measurements depicted in Figure 2a–d. In the SEM top-view images (Figure S2, Supporting Information) of both films we observe that the domain sizes of the perovskite crystals are increased while the surface density of pinholes is decreased for the film treated for 40 min at RT as compared to the film treated for 5 min, leading to an enhanced PCE and reduced hysteresis of the device (Figure S3, Supporting Information).[16] The trend observed for the best device J–V curves, as presented in Figure 4, also holds for averaged devices as shown in Figure S4. Additionally, the greater number of pinholes present in the film treated for 5 min at RT also results in a small open circuit voltage loss due to higher recombination losses, similar to previous results reported in the literature.[31]

In order to investigate the relationship between crystal quality and transport dynamics in our solar cells, we carried out time-of-flight (ToF) studies for the devices fabricated from perovskite films treated for 5 and 40 min at room temperature.

ToF is a well-established method to extract the mobility of charge carriers in semiconductors and solar cells. Based on the generation of charge carriers by short laser pulses and subsequent drifting due to an applied bias, the resulting time-resolved photocurrent is used for the determination of the corresponding mobility.[32] A representative ToF transient is depicted in Figure 4c. From this transient, the transit time t_{tr} is obtained.

For a detailed description of the fitting procedure and the measurement setup used, including the transit time as a function of applied bias, see Figures S5–S7 in the Supporting Information. The time resolution of the system is ~2 ns allowing for the extraction of thin film mobilities after weak excitation following Equation (1):

$$\mu = d^2 / U \cdot t_{tr} \tag{1}$$

Here, d is the active layer thickness and U the applied bias voltage. In the current device structure, we predominantly measure hole transport, as most charges are generated in close proximity to the electron collection layer (TiO_2), while the holes must travel throughout the whole thickness of the film. We note that the resulting ToF transient characteristics in a thin film device fabricated for supporting electron transport, for instance, by using PEDOT:PSS (poly(3,4-ethylenedioxythiophene)-polystyrene sulfonate) and PCBM (phenyl-C_{61}-butyric acid methyl ester), would lead to similar results, since electron and
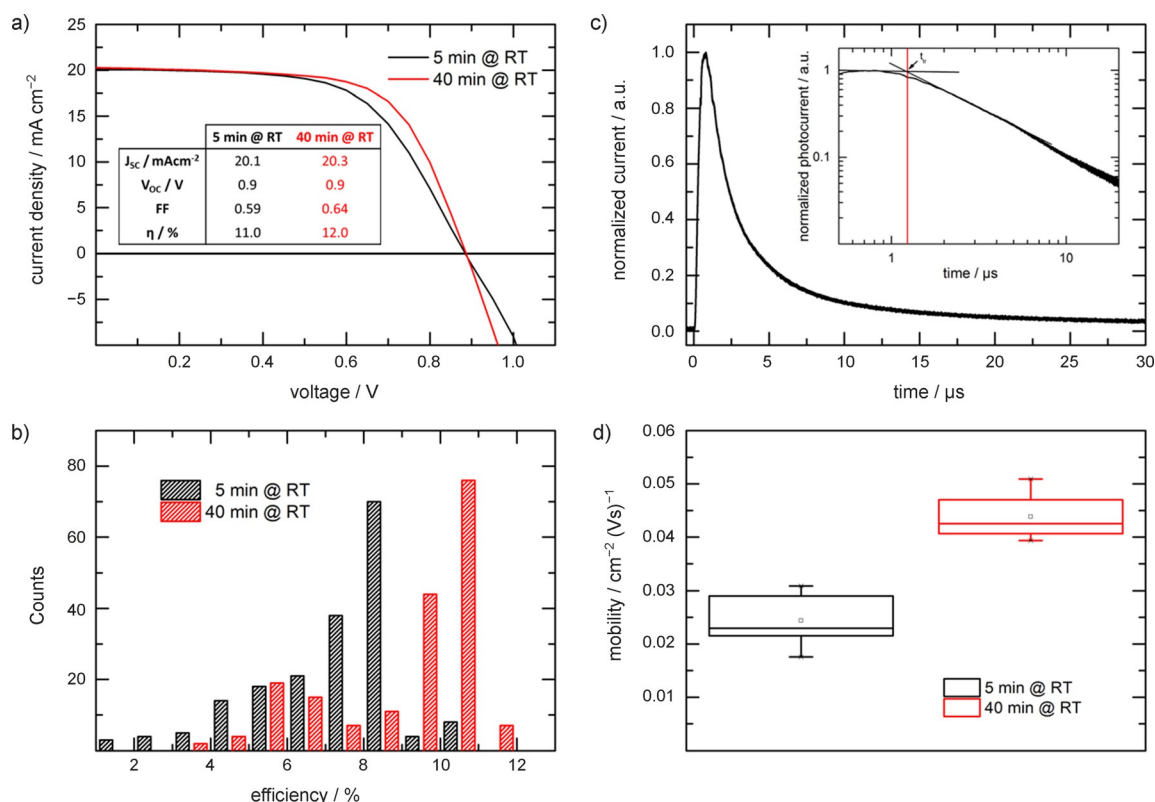
Figure 4. J–V characteristics of $MAPbI_3$-based solar cell devices prepared with 5 min and 40 min evaporation time at RT (a) and their distribution of efficiencies from 200 solar cells (b). Panel c shows a representative ToF transient. The inset is a double logarithmic zoom-in of the region used to fit the data to obtain the transit time t_{tr} (see text). The respective mobilities obtained by ToF measurements of both sample types are depicted in panel d. Here it is observed that the incorporation of the material treated for 40 min at RT in the solar cell leads to an increase in charge-carrier mobility by a factor of 2.

hole mobility in MAPI thin films have been shown to be similar.[33] Further, the penetration depth of light in MAPI thin films at 550 nm is 0.66 µm, as measured by Park.[34]

The results extracted from ToF data can be found in Figure 4d. We note that the experimental error is mainly caused by the determination of the layer thickness. The slow evaporation of the solvent and the associated formation of uniform and big crystals of the perovskite for the 40 min at RT sample can be connected to the enhancement of the mobility of the charge carriers within the photoactive layer, as observed in the ToF measurements. The higher mobility in the 40 min at RT sample is also observable in the J–V characteristic since the series resistance of the solar cell is lowered, which leads to a higher fill factor (FF). The series resistance was estimated by fitting the ohmic regime of the J–V curve and yields 12.5 Ω cm^2 for the 5 min and 8.2 Ω cm^2 for the 40 min device. With this increased conductivity of the sample, the charge extraction by the selective contacts is enhanced, resulting in higher device efficiency. The results presented here show mobility values two orders of magnitude higher than previous ToF studies on perovskite solar cells.[35] We note that the morphology of the perovskite plays an important role for the mobility, as demonstrated here, and hence we expect that the much smaller crystals and thus higher grain boundary density present in the previous study account for the discrepancy. On the other hand, values obtained from THz (8.1 cm^{2}V^{-1}s^{-1})[36] and microwave (6.2 cm^{2}V^{-1}s^{-1})[37] conductivity measurements on the active perovskite layer only are up to three orders of magnitude higher than the present results that have been obtained for complete devices. We attribute these differences to the different transport processes and probing dimensions associated with THz and microwave measurements, in comparison with the complete through-layer transport probed with ToF methods. Moreover, as the ToF measurement probes the entire device, there could also be a minor influence of the transport layer (spiro-OMeTAD) and the relevant interfaces on the apparent mobility of the material.

In summary, we have studied the crystallization of MAPbI$_3$ based on a one-step approach with a chloride-based precursor. Based on in-situ XRD measurements, we propose a crystallization mechanism for the synthesis procedure. Thereby, MAPbCl$_3$ is assembled on the substrate during the slow evaporation of the solvent, and over time some MAPbI$_3$ crystals are also formed. While heating up the substrate, MAPbI$_3$ grows at the expense of MAPbCl$_3$, which leads to crystals oriented parallel to the substrate. Furthermore, we show that a slow evaporation of the solvent during the formation of the MAPbCl$_3$ template influences the morphology, size, and uniformity of the resulting MAPbI$_3$ crystals. Advanced electro-optical characterization by time-of-flight studies in this work showed that the charge-carrier mobility is doubled for devices based on MAPbI$_3$ that were fabricated with more controlled evaporation of the solvent at RT. This indicates that slow evaporation of the solvent before the heat treatment benefits the solar cell efficiency through enhanced conductivity and a corresponding increased device performance.

Experimental Section

Preparation of the precursor: Methylammonium iodide was prepared by adapting a recipe published earlier.[38] In short, 24 mL of methylamine solution (33 % in ethanol, Sigma–Aldrich) was diluted with 100 mL of absolute ethanol in a 250 mL round-bottom flask. To this solution, 10 mL of hydroiodic acid (33 wt %) was added under constant stirring. After a reaction time of one hour at room temperature, the solvents were removed by rotary evaporation. The obtained white solid was washed with dry diethyl ether and finally recrystallized from ethanol.

Solar cell preparation: Fluorine-doped tin oxide (FTO)-coated glass sheets (7 Ω sq^{-1}, Pilkington, USA) were patterned by etching with zinc powder and 3 M HCl. They were subsequently cleaned with a 2 % Hellmanex solution and rinsed with deionized water, ethanol, and acetone. Directly before applying the blocking layer, remaining organic residues were removed by an oxygen plasma treatment for 5 min. The dense TiO$_2$ layer was prepared from a sol-gel precursor solution by spin-coating onto the substrates and calcining at 500 °C in air.[39] For the sol-gel solution a 27.2 mM (70 µL) solution of HCl in 2-propanol (5 mL) was added dropwise to a vigorously stirred 0.43 mM (735 µL) solution of titanium isopropoxide (99.999 %, Sigma–Aldrich) in 2-propanol (5 mL). The solution usually stayed clear during the addition and was discarded otherwise. The precursor solution for the synthesis of MAPbI$_3$ was prepared by dissolving 1.685 g of MAI in 4 mL dry *N,N*-dimethylformamide (DMF, 99.8 %, Sigma–Aldrich). This solution was then added to 973 mg of PbCl$_2$ (98 %, Sigma–Aldrich) and heated to 100 °C in order to fully dissolve the lead precursor. Subsequently, 100 µL of this solution was spin-coated onto the TiO$_2$-covered substrates at 1000 rpm for 45 s. After varying the resting times at RT, the samples were placed on a hotplate at 90 °C for 2 h. Afterwards, two additional heating steps were performed, first 10 min at 100 °C and then 5 min at 130 °C. Next, the films were covered with a layer of Spiro-OMeTAD (Borun Chemicals, 99.5 % purity). Typically, 100 mg of Spiro-OMeTAD were dissolved in 1 mL chlorobenzene (99.8 %, Sigma–Aldrich). The solution was filtered and mixed with 10 µL 4-*tert*-butylpyridine (*t*BP, 96 %, Sigma–Aldrich) and 30 µL of a 170 mg mL^{-1} bis(trifluoromethane)sulfonamide lithium salt (LiTFSI, 99.95 %, Sigma–Aldrich) solution in acetonitrile. This solution was spin-coated dynamically at 1500 rpm for 45 s. In a second step the sample rotation was accelerated to 2000 rpm for 5 s to allow the solvent to dry completely. Before depositing the gold electrodes by evaporation, Spiro-OMeTAD was left to oxidize in air overnight at room temperature and < 20 % rel humidity.

[1] H. J. Snaith, *J. Phys. Chem. Lett.* **2013**, *4*, 3623–3630.

[2] M. Liu, M. B. Johnston, H. J. Snaith, *Nature* **2013**, *501*, 395–398.

[3] J. Burschka, N. Pellet, S.-J. Moon, R. Humphry-Baker, P. Gao, M. K. Nazeeruddin, M. Gratzel, *Nature* **2013**, *499*, 316–319.

[4] S. Kazim, M. K. Nazeeruddin, M. Grätzel, S. Ahmad, *Angew. Chem. Int. Ed.* **2014**, *53*, 2812–2824; *Angew. Chem.* **2014**, *126*, 2854–2867.

[5] M. Xiao, F. Huang, W. Huang, Y. Dkhissi, Y. Zhu, J. Etheridge, A. Gray-Weale, U. Bach, Y.-B. Cheng, L. Spiccia, *Angew. Chem. Int. Ed.* **2014**, *53*, 9898–9903; *Angew. Chem.* **2014**, *126*, 10056–10061.

[6] Z. Xiao, C. Bi, Y. Shao, Q. Dong, Q. Wang, Y. Yuan, C. Wang, Y. Gao, J. Huang, *Energy Environ. Sci.* **2014**, *7*, 2619–2623.

[7] W. Nie, G. Gupta, B. K. Crone, F. Liu, D. L. Smith, P. P. Ruden, C.-Y. Kuo, H. Tsai, H.-L. Wang, H. Li, S. Tretiak, A. D. Mohite, *Adv. Sci.* **2015**, *2*, 1500024.

[8] G. E. Eperon, V. M. Burlakov, P. Docampo, A. Goriely, H. J. Snaith, *Adv. Funct. Mater.* **2014**, *24*, 151.

[9] F. X. Xie, D. Zhang, H. Su, X. Ren, K. S. Wong, M. Grätzel, W. C. H. Choy, *ACS Nano* **2015**, *9*, 639–646.

[10] P. Docampo, J. M. Ball, M. Darwich, G. E. Eperon, H. J. Snaith, *Nat. Commun.* **2013**, *4*, 2761.

[11] M. A. Green, K. Emery, Y. Hishikawa, W. Warta, E. D. Dunlop, *Prog. Photovoltaics* **2015**, *23*, 1.

[12] N. J. Jeon, J. H. Noh, Y. C. Kim, W. S. Yang, S. Ryu, S. I. Seok, *Nat. Mater.* **2014**, *13*, 897–903.

[13] H. Zhou, Q. Chen, G. Li, S. Luo, T.-b. Song, H.-S. Duan, Z. Hong, J. You, Y. Liu, Y. Yang, *Science* **2014**, *345*, 542–546.

[14] M. Saliba, K. W. Tan, H. Sai, D. T. Moore, T. Scott, W. Zhang, L. A. Estroff, U. Wiesner, H. J. Snaith, *J. Phys. Chem. C* **2014**, *118*, 17171–17177.

[15] K. W. Tan, D. T. Moore, M. Saliba, H. Sai, L. A. Estroff, T. Hanrath, H. J. Snaith, U. Wiesner, *ACS Nano* **2014**, *8*, 4730–4739.

[16] W. Nie, H. Tsai, R. Asadpour, J.-C. Blancon, A. J. Neukirch, G. Gupta, J. J. Crochet, M. Chhowalla, S. Tretiak, M. A. Alam, H.-L. Wang, A. D. Mohite, *Science* **2015**, *347*, 522–525.

[17] X. Wu, M. T. Trinh, D. Niesner, H. Zhu, Z. Norman, J. S. Owen, O. Yaffe, B. J. Kudisch, X. Zhu, *J. Am. Chem. Soc.* **2015**, *137*, 2089–2096.

[18] N. K. Noel, A. Abate, S. D. Stranks, E. Parrott, V. Burlakov, A. Goriely, H. J. Snaith, *ACS Nano* **2014**, *8*, 9815–9821.

[19] F. K. Aldibaja, L. Badia, E. Mas-Marza, R. S. Sanchez, E. M. Barea, I. Mora-Sero, *J. Mater. Chem. A* **2015**, *3*, 9194–9200.

[20] Y. Li, W. Sun, W. Yan, S. Ye, H. Peng, Z. Liu, Z. Bian, C. Huang, *Adv. Funct. Mater.* **2015**, *25*, 4867.

[21] V. L. Pool, A. Gold-Parker, M. D. McGehee, M. F. Toney, *Chem. Mater.* **2015**, *27*, 7240–7243.

[22] P. Docampo, F. Hanusch, S. D. Stranks, M. Döblinger, J. M. Feckl, M. Ehrensperger, N. K. Minar, M. B. Johnston, H. J. Snaith, T. Bein, *Adv. Energy Mater.* **2014**, *4*, 1400355.

[23] A. E. Williams, P. J. Holliman, M. J. Carnie, M. L. Davies, D. A. Worsley, T. M. Watson, *J. Mater. Chem. A* **2014**, *2*, 19338–19346.

[24] J. S. Manser, B. Reis, P. V. Kamat, *J. Phys. Chem. C* **2015**, *119*, 17065–17073.

[25] H. P. Wirges, *Chem. Ing. Tech.* **1995**, *67*, 1513–1514.

[26] C. Huang, N. Fu, F. Liu, L. Jiang, X. Hao, H. Huang, *Sol. Energy Mater. Sol. Cells.* **2016**, *145*, 231–237.

[27] W. Ostwald, *Z. Phys. Chem.* **1897**, *22*, 289–330.

[28] L. Chi, I. Swainson, L. Cranswick, J.-H. Her, P. Stephens, O. Knop, *J. Solid State Chem.* **2005**, *178*, 1376–1385.

[29] C. C. Stoumpos, C. D. Malliakas, M. G. Kanatzidis, *Inorg. Chem.* **2013**, *52*, 9019–9038.

[30] D. Liu, T. L. Kelly, *Nat. Photonics* **2014**, *8*, 133–138.

[31] G. E. Eperon, V. M. Burlakov, P. Docampo, A. Goriely, H. J. Snaith, *Adv. Funct. Mater.* **2014**, *24*, 151–157.

[32] S. Tiwari, N. C. Greenham, *Opt. Quantum Electron.* **2009**, *41*, 69–89.

[33] D. Shi, V. Adinolfi, R. Comin, M. Yuan, E. Alarousu, A. Buin, Y. Chen, S. Hoogland, A. Rothenberger, K. Katsiev, Y. Losovyj, X. Zhang, P. A. Dowben, O. F. Mohammed, E. H. Sargent, O. M. Bakr, *Science* **2015**, *347*, 519–522.

[34] N. G. Park, *Mater. Today* **2015**, *18*, 65–72.

[35] Y. Chen, J. Peng, D. Su, X. Chen, Z. Liang, *ACS Appl. Mater. Interfaces* **2015**, *7*, 4471–4475.

[36] C. Wehrenfennig, G. E. Eperon, M. B. Johnston, H. J. Snaith, L. M. Herz, *Adv. Mater.* **2014**, *26*, 1584–1589.

[37] T. J. Savenije, C. S. Ponseca, L. Kunneman, M. Abdellah, K. Zheng, Y. Tian, Q. Zhu, S. E. Canton, I. G. Scheblykin, T. Pullerits, A. Yartsev, V. Sundström, *J. Phys. Chem. Lett.* **2014**, *5*, 2189–2194.

[38] M. M. Lee, J. Teuscher, T. Miyasaka, T. N. Murakami, H. J. Snaith, *Science* **2012**, *338*, 643.

[39] J. M. Ball, M. M. Lee, A. Hey, H. J. Snaith, *Energy Environ. Sci.* **2013**, *6*, 1739–1743.